Structure and control of charge density waves in two-dimensional 1T-TaS$_2$

Adam W. Tsen[a], Robert Hovden[b], Dennis Wang[c], Young Duck Kim[d], Junichi Okamoto[e], Katherine A. Spoth[b], Yu Liu[f], Wenjian Lu[f], Yuping Sun[f,g,h], James C. Hone[d], Lena F. Kourkoutis[b,i], Philip Kim[a,j,1], and Abhay N. Pasupathy[a,1]

[a]Department of Physics, Columbia University, New York, NY 10027; [b]School of Applied and Engineering Physics, Cornell University, Ithaca, NY 14853; [c]Department of Applied Physics and Applied Mathematics, Columbia University, New York, NY 10027; [d]Department of Mechanical Engineering, Columbia University, New York, NY 10027; [e]Department of Physics, University of Hamburg, D-20355 Hamburg, Germany; [f]Key Laboratory of Materials Physics, Institute of Solid State Physics, Chinese Academy of Sciences, Hefei 230031, People's Republic of China; [g]High Magnetic Field Laboratory, Chinese Academy of Sciences, Hefei 230031, People's Republic of China; [h]Collaborative Innovation Centre of Advanced Microstructures, Nanjing University, Nanjing 210093, People's Republic of China; [i]Kavli Institute at Cornell for Nanoscale Science, Ithaca, NY 14853; and [j]Department of Physics, Harvard University, Cambridge, MA 02138

The layered transition metal dichalcogenides host a rich collection of charge density wave phases in which both the conduction electrons and the atomic structure display translational symmetry breaking. Manipulating these complex states by purely electronic methods has been a long-sought scientific and technological goal. Here, we show how this can be achieved in 1T-TaS$_2$ in the 2D limit. We first demonstrate that the intrinsic properties of atomically thin flakes are preserved by encapsulation with hexagonal boron nitride in inert atmosphere. We use this facile assembly method together with transmission electron microscopy and transport measurements to probe the nature of the 2D state and show that its conductance is dominated by discommensurations. The discommensuration structure can be precisely tuned in few-layer samples by an in-plane electric current, allowing continuous electrical control over the discommensuration-melting transition in 2D.

two-dimensional materials | strongly correlated systems | charge density waves

Layered 1T-TaS$_2$ exhibits a number of unique structural and electronic phases. At low temperature and ambient pressure, the ground state is a commensurate (C) charge density wave (CDW). On heating, it undergoes a sequence of first-order phase transitions to a nearly commensurate (NC) CDW at 225 K, to an incommensurate (IC) CDW at 355 K, and finally to a metallic phase at 545 K. Each transition involves both conduction electron and lattice degrees of freedom—large changes in electronic transport properties occur, concomitant with structural changes to the crystal. By either chemical doping or applying high pressures, it is possible to suppress the CDWs and induce superconductivity (1–3). For device applications, it is desirable to control these phases by electrical means, but this capability is difficult to achieve in bulk crystals due to the high conduction electron density. Recent efforts to produce thin samples by mechanical exfoliation provide a new avenue for manipulating the CDWs in 1T-TaS$_2$ (4–8). These studies have demonstrated the suppression of CDW phase transitions using polar electrolytes, as well as resistive switching between the different phases. As the material approaches the 2D limit, however, significant changes have been observed in the transport properties (4, 5, 8). However, the microscopic nature of the 2D state remains unclear. In this work, we use transmission electron microscopy (TEM) together with transport measurements to develop a systematic understanding of the CDW phases and phase transitions in ultrathin 1T-TaS$_2$. We find that charge ordering disappears in flakes with few atomic layers due to surface oxidation. When samples are instead environmentally protected, the CDWs persist and their transitions can be carefully tuned by electric currents.

Both the atomic and CDW structure of 1T-TaS$_2$ can be visualized in reciprocal space by TEM electron diffraction (9, 10). In Fig. 1A, we show diffraction images taken from a bulk-like, 50-nm-thick

crystal at low and room temperature (C phase, blue panel; NC phase, red panel). The bright peaks (connected by dashed lines) correspond to Bragg scattering from a triangular lattice of Ta atoms with lattice constant $a = 3.36$ Å. Additional weaker diffraction peaks appear from the periodic atomic displacements of the CDW. In the low-temperature C phase, Ta atoms displace to make Star-of-David clusters (blue inset, Fig. 1B). The outer 12 atoms within each star displace slightly inward toward the atom at the center, giving rise to a commensurate superstructure with wavelength $\lambda_C = \sqrt{13}a$ that is rotated $\phi_C = 13.9°$ with respect to the atomic lattice. The NC phase at room temperature also consists of such 13-atom distortions. Scanning tunneling microscope (STM) measurements have revealed, however, that such ordering is only preserved in quasi-hexagonal domains consisting of tens of stars (11, 12), with domain periodicity 60–90 Å depending on temperature (13, 14). The domains are separated by a discommensuration network forming a Kagome lattice, inside of which the Ta displacements are substantially reduced (15). A schematic of this structure is shown in the red inset of Fig. 1B.

When ultrathin 1T-TaS$_2$ crystals (approximately <5 nm thickness) are exfoliated in an ambient air environment, the CDW structure is not observed by the TEM electron diffraction. In the left panel of Fig. 1C, we show a room temperature electron diffraction pattern taken on a few-layer flake. The presence of Bragg peaks without CDW scattering suggests that the 1T-TaS$_2$ layers are in a phase that

Significance

The ability to electrically control collective electron states is a central goal of materials research and may allow for the development of novel devices. 1T-TaS$_2$ is an ideal candidate for such devices due to the existence of various charge ordered states in its phase diagram. Although various techniques have been demonstrated to manipulate charge order in 1T-TaS$_2$, a fundamental understanding of the effects is still lacking, and the methods used are incompatible with device fabrication. By using both high-resolution transmission electron microscopy and electronic transport to investigate atomically thin 1T-TaS$_2$ samples, we clarify the microscopic nature of the charge ordered phases in the 2D limit and further control them by all-electrical means.
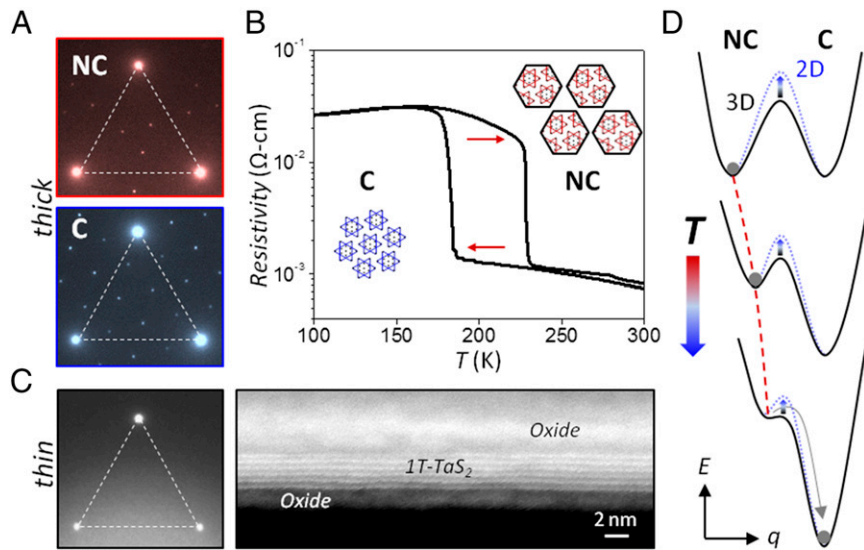
Fig. 1. NC-C CDW phase transition in bulk 1T-TaS$_2$ and CDW suppression by oxidation in thin flakes. (*A*) TEM diffraction images of 50-nm-thick 1T-TaS$_2$ at 295 K (red, NC phase) and 100 K (blue, C phase). Weaker peaks are due to CDW distortion. (*B*) Resistivity vs. temperature of bulk 1T-TaS$_2$ crystal around the first-order, NC-C transition. (*Insets*) Real space schematics of CDW structure. (*C*) (*Left*) TEM diffraction of few-layer 1T-TaS$_2$ flake shows absence of CDW order. (*Right*) High-resolution, cross section electron microscopy image reveals presence of amorphous oxide. (*D*) Free energy schematic of CDW evolution with temperature. Vertical and horizontal axis represent free energy (*E*) and reaction coordinate (*q*), respectively. NC domains grow slowly upon cooling until abrupt transition into the C phase. Energy barrier increases in 2D samples protected from oxidation.

is not observed in bulk crystals at this temperature. High-resolution electron microscopy and energy dispersive spectroscopy on fully suspended samples reveal a strong presence of oxidation as well as an amorphous layer on the surface (Figs. S1 and S2). The amorphous oxide (~2 nm thickness) can be clearly seen atop both surfaces of the 1T-TaS$_2$ layers in cross section (Fig. 1*C*, *Right*). It is possible that oxidation leads to strong surface pinning, which destroys charge ordering in ultrathin samples. Recent resistivity measurements on exfoliated 1T-TaS$_2$ crystals have also reported the disappearance of CDWs in sufficiently thin flakes (5). It is not clear, however, whether these are intrinsic effects related to dimensionality or extrinsic consequences of oxidation.

To prevent surface oxidation, we exfoliated 1T-TaS$_2$ crystals within a nitrogen-filled glove box with under 2-ppm oxygen concentration. The flakes were protected by a capping layer of thin hexagonal boron nitride (hBN) before transfer out into the ambient environment (*Methods*). TEM diffraction performed on these protected samples reveals that CDW formation persists down to the lowest thicknesses measured (2 nm), as we discuss in detail in Fig. 4. This finding indicates that the absence of charge order in ultrathin, uncovered flakes is most likely caused by the effects of oxidation. The study and utilization of CDWs in 2D 1T-TaS$_2$ thus requires careful sample preparation in inert atmosphere.

The different structural phases of 1T-TaS$_2$ exhibit distinct electronic transport properties that may be exploited for device applications. In the main panel of Fig. 1*B*, we show temperature-dependent resistivity of a bulk crystal measured across the NC-C phase transition. Resistivity abruptly increases (decreases) by over an order of magnitude on entering the C (NC) phase. The hysteresis loop between cooling and warming defines the temperature region of metastability between the two phases and can be understood by a free energy picture (Fig. 1*D*). In a first-order transition, an activation barrier separates the stable energy minima corresponding to the NC and C states. With cooling from the NC phase, both the C state energy and the height of the barrier decrease with respect to the NC energy. When the C state has lower energy, the NC phase becomes metastable, but the system only transitions into the C phase when the activation barrier becomes comparable to the thermal energy. The situation is reversed when

warming from the C phase. In oxidation-free 2D samples, this electronic transition is qualitatively unchanged.

Fig. 2*A* shows an example of hBN-encapsulated 1T-TaS$_2$ flakes before (*Upper*) and after device fabrication (*Lower*). To make electrical contact to the covered samples, we used a technique of edge metallization developed for graphene/hBN heterostructures (*Methods*) (16). A side-view device schematic is shown in the *Inset* of the lower panel. In the main panel of Fig. 2*B* (*I* = 0, black curve), we plot resistance as a function of temperature for a 4-nm-thick sample measured across the NC-C phase transition. The behavior is similar to that of the bulk crystal (Fig. 1*B*); however, the hysteretic region between cooling and warming is substantially widened, indicating that one or both of the CDW phases become more metastable.

Metastable phases of a CDW system are generally more susceptible to electronic perturbations, because CDWs directly couple to electric field (6–8, 17). In our device, we observe that continuous current flow stabilizes the NC phase at low temperatures. In Fig. 2*B* (main panel), we show ac resistance with temperature while also applying a continuous, in-plane dc current, starting at room temperature (300 K). As the dc current *I* is increased, the final resistance at low temperature is monotonically lowered. Concomitant with this trend, the resistance jump resulting from the NC-C phase transition also decreases with increasing *I*. In the *Inset*, we plotted the ratio of the resistance difference between cooling and warming, ΔR, to resistance *R* in the more conducting state at *T* = 180 K, the temperature in the middle of the hysteresis region, as a function of the dc current level. For *I* = 35 µA (blue curve in main panel), the NC-C phase transition is completely absent. This measurement indicates that C phase formation in the current driven sample is very different compared with the zero-current, equilibrium condition. Current flow hinders the formation of the C phase and maintains the sample in the more conductive NC state at low temperature. We exclude Joule heating of the sample as a possible explanation by slowly turning off the current at low temperature and verifying that the resistance does not change. We also note that cooling and warming the sample again without dc current flow reproduces the original phase transitions (Fig. S3), indicating that the currents have not damaged the flake irreversibly.

PHYSICS
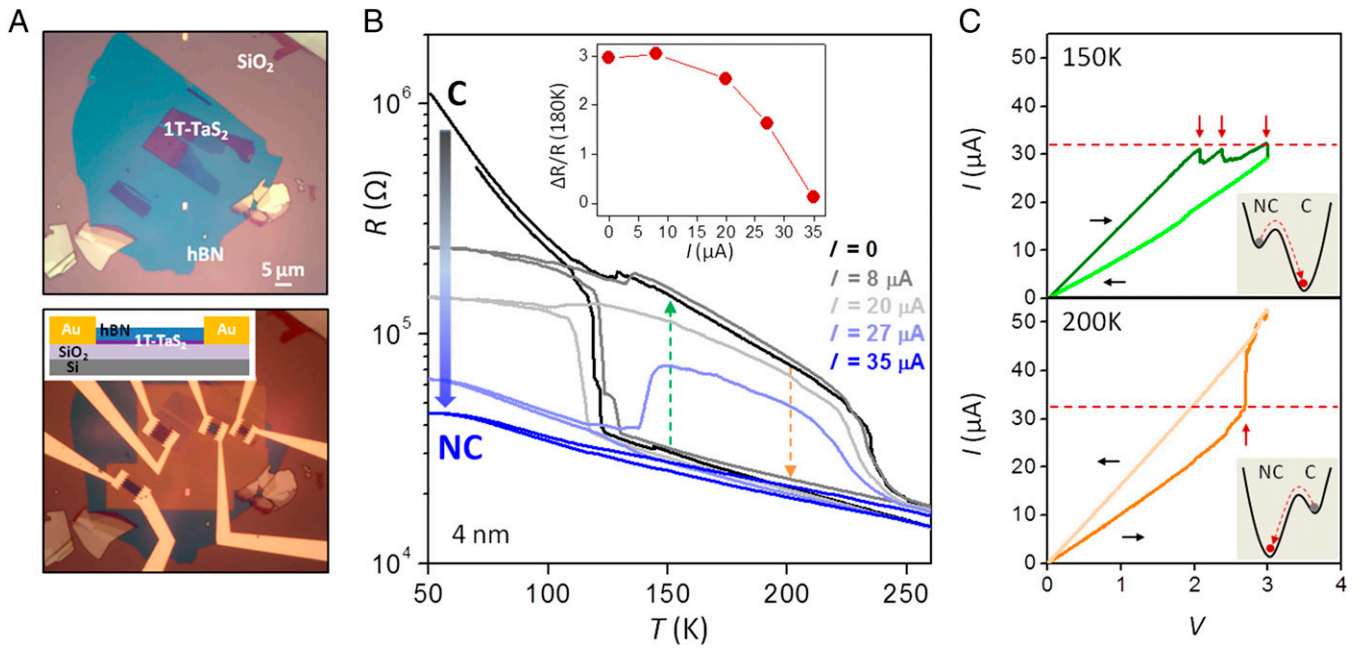
Fig. 2. Electrical control of NC-C transition in oxidation-free, 2D devices. (*A*) Optical images of 1T-TaS$_2$ flakes on a SiO$_2$/Si wafer covered by hBN in inert atmosphere before (*Upper*) and after (*Lower*) side electrical contact. (*Inset*) Side-view device schematic. (*B*) ac resistance vs. temperature for 4-nm-thick device as a function of dc current. Continuous current flow stabilizes NC phase at low temperature. Normalized resistance difference between cooling and warming is plotted as a function of dc current in *Inset*. (*C*) (*Upper*) Current vs. voltage sweep at 150 K starting in NC phase shows abrupt decreases in current and transition to the C phase. (*Lower*) Same at 200 K starting in C phase shows abrupt increase in current and transition to NC phase. Sweep rate is 3–6 V/min. Free energy schematics of electrically induced transitions are plotted in *Insets*.

Our observation suggests that it is possible to maintain the NC phase in a temperature region where it is not thermodynamically stable. We now show that the opposite phenomenon is also possible, i.e., we can drive a transition toward the thermodynamically stable state, if we apply an in-plane current after cooling or warming the sample in equilibrium. Fig. 2*C* shows the current induced phase transitions in the same device (4 nm thickness). Here, we start in the NC phase at room temperature and cool the sample down to 150 K without current flow. At this temperature, although the sample remains in the NC state, the NC phase is now metastable, and the C phase is the thermodynamically stable state. As we increase the voltage across the device (upper panel, dark green curve), the measured current through the device decreases in abrupt steps (marked by red arrows) when it reaches a critical current $I_c \sim 30$ μA (marked by red dashed line). On sweeping the bias current back to zero (light green curve), the device remains in a more insulating state. Warming up the sample after this point produces a temperature curve similar to the C phase, and a transition to the NC phase is observed. We have demonstrated that a bias current applied to the sample can be used to drive the metastable NC phase toward the thermodynamically preferred C state. The dashed green arrow in Fig. 2*B* marks the direction of this current-induced NC to C phase transition and a free energy schematic of this process is shown in the *Inset* of the upper panel of Fig. 2*C*.

Similarly, the metastable C state can also be driven toward the NC phase with current. Here, we start in the C phase at 50 K and warm up to 200 K. The sample remains in the C phase, but now the NC phase is the thermodynamic ground state. As shown in the lower panel of Fig. 2*C*, sweeping the voltage in this case results in a sharp increase in current and drives the sample toward the more conducting NC state. We have used the dashed orange arrow in Fig. 2*B* and the free energy picture in the inset of the lower panel of Fig. 2*C* to represent this opposite C to NC transition. Interestingly, both induced transitions occur when the

current reaches about $I_c \sim 30$ μA, indicating that indeed current flow rather than electric field is the underlying mechanism that drives the transition. We repeated this measurement at various temperatures and initial conditions. In all cases, whenever the initial system is metastable, reaching a current threshold of 30 to 40 μA drives the system toward the thermodynamically stable state, regardless of device resistance. In contrast, we observe no induced transition up to 45 μA at 260 K, where a metastable phase ceases to exist.

Taken together, the results of Fig. 2 demonstrate that it is possible to electrically control the NC-C transition in 2D 1T-TaS$_2$, where the temperature region of metastability is significantly enhanced. A more detailed study of this phase transition in 2D samples, however, can provide a better understanding of our experimental observations. The key structural difference between the two CDW phases is the presence of the discommensuration network in the NC phase (Fig. 1*B*, red inset). The NC-C transition can then be interpreted as a discommensuration-melting transition, which can be significantly affected by dimensionality (18, 19). The discommensurations have a striking effect on the electronic transport properties in 1T-TaS$_2$. The NC phase is an order of magnitude more conductive than the C phase. If we assume that the interior of each commensurate domain has similar transport properties as the C phase, this then implies the discommensuration regions in the NC phase are at least 10 times more conductive than the domain interior (3). Such a view is supported by the fact that the atomic structure within the discommensurations is close to the high-temperature metallic phase (15). With this interpretation, we can use transport measurements to better understand the role of dimensionality on the discommensuration-melting transition.

As the number of 1T-TaS$_2$ layers decreases, the resistivity change corresponding to the NC-C phase transition evolves in a continuous manner down to 2 nm thickness in environmentally protected samples. Fig. 3*A* shows resistivity as a function of temperature for four hBN-covered 1T-TaS$_2$ flakes, all measured using
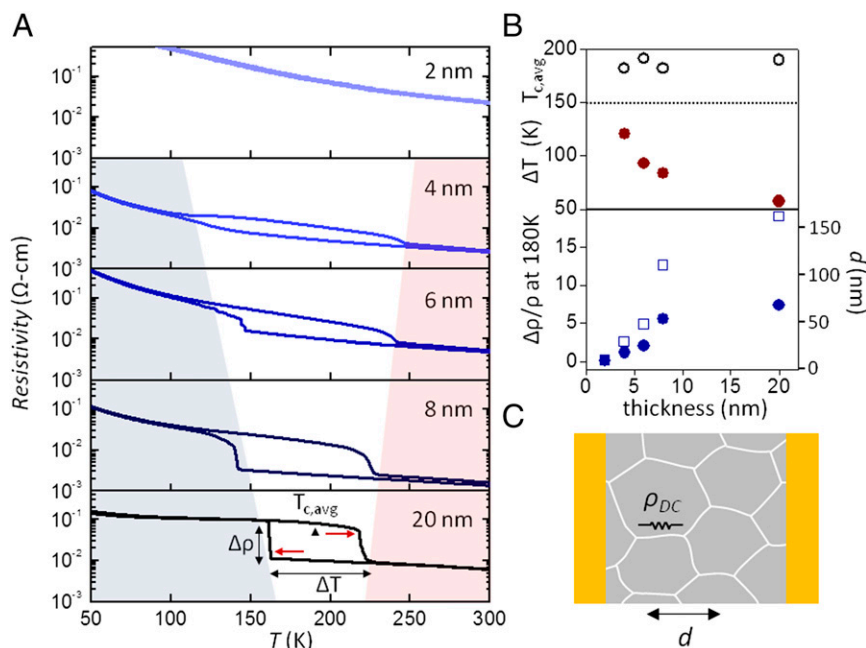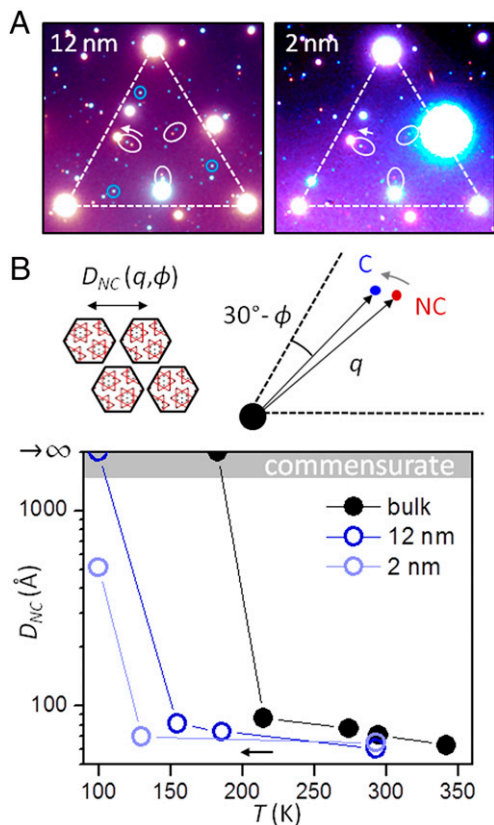
Fig. 3. Dimensional dependence of phase transition—electron transport. (*A*) Thickness evolution of temperature-dependent resistivity around NC-C phase transition measured on hBN-covered ultrathin samples and 20-nm-thick flake. (*B*) Average transition temperature and temperature hysteresis (*Upper*) and normalized resistivity difference (*Lower*) between cooling and warming as a function of sample thickness. Open squares are corrections from contact resistance (Fig. S4). Hysteresis widens and resistivity difference decreases in thinner samples, whereas average transition temperature remains constant. Resistivity change can be used to estimate the discommensuration density $1/d$ at low temperature. (*C*) Circuit model of discommensuration network.

a 1 K/min sweep rate. Their thicknesses are 2, 4, 6, and 8 nm as determined using an atomic force microscope. For comparison, we show data from an unprotected, 20-nm-thick flake, which exhibits characteristics similar to the bulk crystal, indicating that the effects of oxidation are less pronounced in thicker samples. The temperature hysteresis associated with the phase transition between cooling and warming is substantially increased in thinner samples, consistent with our earlier observations of the device in Fig. 2*A*. The progressive widening of the hysteresis loop continues down to the 4-nm-thick device, below which there is no longer a detectable transition. A guide to the eye for the expansion of this metastable region is shown by the colors in Fig. 3*A*. In the upper panel of Fig. 3*B*, we plot $\Delta T = T_{c,warm} - T_{c,cool}$ as a function of flake thickness, where $T_{c,warm}$ and $T_{c,cool}$ are the experimentally observed NC to C or C to NC transition temperature during the warming or cooling process, respectively. Here, T_c is determined by the temperature at which the first derivative peaks in the temperature sweep. ΔT is 60 K for the 20-nm flake, slightly larger than that for the bulk crystal (40 K), and grows to 120 K for the 4-nm device. In the same panel, we also plot the average temperature $T_{c,avg} = (T_{c,warm} + T_{c,cool})/2$ of the transition. $T_{c,avg}$ does not change substantially with thickness and remains between 180 and 190 K, which then implies that lower dimensionality does not stabilize either the NC or C phase. Instead, the NC (C) phase becomes increasingly metastable during cooling (warming) for thinner samples, indicating that the size of the energy barrier separating the NC and C phases increases (Fig. 1*D*).

Although ΔT increases when sample thickness is reduced, the resistivity jump associated with the phase transition decreases with decreasing thickness. In the bottom panel of Fig. 3*B*, we plot the resistivity difference $\Delta\rho$ between cooling and warming at $T = 180$ K, normalized to ρ in the more conducting state as a function of flake thickness. The closed circles are extracted directly from the data in Fig. 3*A*, whereas the open squares are corrections due to the effects of contact resistance (Fig. S4). For the 20-nm device, resistivity changes by an order of magnitude. The change is

smaller for thinner devices and disappears completely for the 2-nm device, which indicates that more conducting NC discommensurations persist at low temperatures for thinner samples, consistent with the larger energy barriers required to remove them. Also, the resistivity jump becomes less abrupt, which is a reflection that the phase transition has slowed, as larger energy barriers generally act also to impede the kinetics of a phase transition. A simple circuit model presented in Fig. 3*C* allows us to connect the measured resistance jump in the NC-C transition, ΔR, with the estimated density of discommensurations $1/d$ left in the low temperature phase. We assume that the device resistance at low temperature is dominated by conduction through a random network of discommensuration channels (shown as white lines), which is generally sensitive to the particular microstructure formed. However, for device sizes much larger than d, we find the resistance with discommensuration channels would be $R \sim \rho_{DC}\, d$, where ρ_{DC} is the resistivity per unit length of each discommensuration channel. Similarly, in the high temperature NC phase with a well-defined discommensuration network, we have $R_{NC} \sim \rho_{DC}\, D_{NC}$, where we assume $D_{NC} \sim 80$ Å (13, 14). From this, we can use the resistivity change in Fig. 3*B* to determine d: $(\Delta R/R_{NC}) \sim (d/D_{NC}) - 1$. On the right axis, we plotted d extracted for the different sample thicknesses. For the 2-nm sample, $d \sim D_{NC}$, whereas it grows to 70–160 nm for the 20-nm sample.

We can further substantiate the microscopic picture presented above by providing atomic structural analysis based on TEM. As before, the CDW structure is preserved by environmentally controlled hBN encapsulation. In Fig. 4*A*, we show diffraction images taken from two 1T-TaS$_2$ flakes of different thicknesses (12 and 2 nm). To highlight their temperature dependence, we have overlaid the diffraction patterns for each flake at 295 K (red peaks) and 100 K (blue peaks), our lowest achievable temperature. Ta Bragg peaks are again connected by a dashed triangle. Multiple scattering from hBN creates additional discernable peaks. The CDW peaks have been circled for easy identification. Although the peaks circled in gray appear qualitatively similar for

PHYSICS

Fig. 4. Dimensional dependence of phase transition—electron diffraction. (*A*) Overlaid TEM diffraction images of ultrathin 1T-TaS$_2$ covered with hBN taken at 295 K (red peaks) and 100 K (blue peaks) for two flake thicknesses. hBN preserves CDW order (circled peaks) but introduces additional diffraction spots. (*B*) (*Upper Right*) Zoom-in schematic of CDW diffraction peaks showing temperature evolution. Position of NC spot can be used to estimate commensurate domain periodicity D_{NC} (*Upper Left*). (*Lower*) D_{NC} vs. temperature with cooling measured for the two covered samples compared with data reproduced from ref. 14. Reduced thickness pushes NC to C phase transition to lower temperature.

both flakes, only the thicker flake displays additional peaks (circled in blue) at 100 K, indicating that it makes the transition to the C phase (compare with blue panel in Fig. 1*A*), whereas the thinner flake remains in the NC phase. This observation is consistent with our transport data as larger energy barriers in thinner samples require lower temperatures to realize the C phase.

The movement of the gray-circled peaks with cooling (denoted by arrows, Fig. 4*A*) can be understood more quantitatively with reference to the zoom-in schematic shown in Fig. 4*B* (*Upper Right*). The position of this CDW peak is related to the periodicity D_{NC} of the NC domains (*Upper Left*) by a simple geometric expression (14): $D_{NC} = a/\sqrt{(2\pi\Delta\phi/360°)^2 + (\Delta\lambda/\lambda_C)^2}$, where $\Delta\phi$ is the difference in degrees between ϕ and $\phi_C = 13.9°$, and $\Delta\lambda$ is the difference between the apparent wavelength averaged over many domains and $\lambda_C = \sqrt{13}a$. Thus, as the domain size grows, the NC peaks move closer to the C phase positions. We explicitly measured the position and angle of the CDW wave vectors for these two samples at several different temperatures during cooling to determine the domain period D_{NC} using the expression above. The results are plotted in the lower panel of Fig. 4*B*. For comparison, we also reproduce STM results obtained by Thomson et al. on the surface of a bulk crystal (14). For bulk samples, D_{NC} grows steadily from 60 to 90 Å on cooling from 340 to 215 K and then jumps to an arbitrarily large value on transition into the C phase at ~180 K. At the same time, the width of the discommensuration

regions remains relatively constant (~22 Å) in all of the NC phase (13). As with our transport results, we find that reducing sample thickness suppresses the NC to C phase transition to lower temperatures during cooling and slows the CDW domain growth rate during the transition. For both of the thin flakes, the initial domain size at room temperature is similar to that that of the bulk crystal (D_{NC} = 60–70 Å). D_{NC} increases slightly upon cooling in the NC phase. For the 12-nm flake, the C phase is formed between 100 and 150 K, whereas the 2-nm flake remains in the NC phase even at 100 K. Its domain size here is much larger ($D_{NC} \sim 500$ Å), however, indicating that the phase transition has begun to take place. This result is in clear contrast to bulk samples where the transition is abrupt.

Our transport and TEM measurements both indicate that reduced dimensionality increases the energy barrier separating the NC and C CDW phases and thus widens the metastable region of the phase transition. The transition into the C phase involves melting or removal of the NC discommensuration network. Microscopically, energy barriers to discommensuration motion have been attributed to the presence of defects or impurities in the material, which act to pin them locally (20). Even in nominally pure CDW samples, clusters of localized defects have been observed by STM (21, 22), where the distance between defects is on the order of ~10 nm. In bulk 1T-TaS$_2$, the interlayer stacking of NC domains make the discommensuration walls extended planar objects (15, 23), which are generally more difficult to pin. In two dimensions, however, the discommensurations become lines, which may be more easily immobilized. We have constructed a model of discommensuration pinning for a 2D system of thickness t (Fig. S5). We find that in the ultrathin limit where t is smaller than the mean distance between impurities, the pinning energy for a discommensuration plane scales as $E_{pin} \sim t^{-2/3}$, corresponding to a cross-over from collective weak pinning to strong individual pinning. These strong pinning centers stabilize the NC discommensuration network at low temperatures during cooling and will also hinder the nucleation and growth of discommensurations when warming from the C phase, thus increasing the temperature region of metastability for both CDW phases in accordance with our experimental observation.

By using this microscopic understanding of the NC-C phase transition in 2D samples, we may further elucidate the role of dc current in the measurements of Fig. 2 *B* and *C*. When the sample is cooled in equilibrium starting in the NC phase, the activation barrier between the NC and C states is continuously lowered, and therefore discommensurations are driven away and domain size grows steadily. Near the transition temperature, the small barrier can then be overcome with sufficient current flow, which depins the discommensurations to form the C phase ground state (Fig. 2*C*). On the other hand, when the sample is cooled out of equilibrium in the presence of a large dc current, it is likely that the domain size does not grow—the activation barrier remains large and the small-domain NC state persists on cooling to the lowest temperatures (Fig. 2*B*). The dc current is thus effectively a way to control the activation barrier between the NC and C phases.

Although a spatially resolved study is still needed to fully understand these effects, our results have both clarified the nature of the 2D state in 1T-TaS$_2$ and demonstrated clear electrical control over the NC-C phase transition in ultrathin samples, further establishing the material's relevance for device applications. We also expect our environmentally controlled techniques to be applicable for the study of other 2D transition-metal dichalcogenides that may be unstable under ambient conditions (24).

Methods

Synthesis of 1T-TaS$_2$. High-quality single crystals of 1T-TaS$_2$ were grown by the chemical vapor transport (CVT) method with iodine as a transport agent. The high-purity Ta (3.5 N) and S (3.5 N) were mixed in chemical stoichiometry and

heated at 850 °C for 4 d in an evacuated quartz tube. The harvested TaS_2 powders and iodine (density: 5 mg/cm^3) were then sealed in an another quartz tube and heated for 2 wk in a two-zone furnace, in which the source zone and growth zone were fixed at 900 °C and 800 °C, respectively. The tubes were rapidly quenched in cold water to ensure retaining of the 1T phase.

Device Assembly and Fabrication. We exfoliated thin $1T\text{-}TaS_2$ flakes onto SiO_2/Si wafers inside a N_2-filled glovebox containing below 2 ppm O_2 concentration. Outside the glovebox we separately exfoliated single-crystal hBN flakes onto SiO_2/Si. Using a polydimethylsiloxane (PDMS) stamp covered with polypropylene carbonate (PPC), we picked up thin hBN (<30 nm thickness) via the method described in Wang et al. (16). This sample was then moved inside the glovebox. To prepare the $1T\text{-}TaS_2$ for TEM study, we used the hBN to again pick up $1T\text{-}TaS_2$ in situ and then transfer the hBN/$1T\text{-}TaS_2$ stack onto a TEM chip with a SiN membrane. The chip was then moved outside of the glovebox and cleaned in acetone, followed by isopropanol.

To prepare $1T\text{-}TaS_2$ for transport studies, we again exfoliated flakes on SiO_2/Si inside the glovebox. hBN was used to cap $1T\text{-}TaS_2$ in a manner similar to that described above. First, electron beam resist (950PMMA A6, thickness ~300 nm) was used as an etch mask to define the device channel. The pattern was written using a 30-keV electron beam lithography system with an exposure dosage between 300 and 450 μC/cm^2. Afterward, the stack was etched in an Oxford ICP 80 system using plasma generated from a mixture of O_2 and CHF_3 gases with a flow rate of 4 and 40 sccm, respectively. This etch leaves $1T\text{-}TaS_2$ exposed at the edges of the channel. We found a 1-min etch time can completely etch away flakes under 10 nm thickness.

A subsequent lithography step was then used to pattern metal electrodes contacting the $1T\text{-}TaS_2$ edge. We performed a second identical etch immediately before metal evaporation (1 nm Cr/50 nm Au) to expose a new edge

with reduced oxidation. Alternatively, we also picked up thin $1T\text{-}TaS_2$ with hBN/graphene heterostructures and placed the entire stack on another hBN substrate. Here, few-layer graphene was used as electrodes to contact the top surface of $1T\text{-}TaS_2$. We see no substantial difference in the temperature-dependent resistivity behavior between these two processes.

SEM/TEM. The conventional TEM experiments, including electron diffraction, were conducted on an FEI T12 Bio-Twin operating at 80 keV. Temperatures as low as ~97 K were accessible using a cryogenic specimen stage. A high vacuum environment and the microscope's fixed cryo-shields prevented accumulation of ice on the specimen when held at low temperatures. High-resolution scanning TEM images were collected on a FEI Tecnai F20 transmission electron microscope operating at 200 keV with a probe forming semiangle of roughly 9.6 mrad and a high-angle annular dark field detector at a camera length of 150 mm.

1. Li LJ, et al. (2012) Fe-doping–induced superconductivity in the charge-density-wave system 1T-TaS$_2$. *Europhys Lett* 97(6):67005.
2. Liu Y, et al. (2013) Superconductivity induced by Se-doping in layered charge-density-wave system 1T-TaS$_{2-x}$Se$_x$. *Appl Phys Lett* 102(19):192602.
3. Sipos B, et al. (2008) From Mott state to superconductivity in 1T-TaS$_2$. *Nat Mater* 7(12):960–965.
4. Yoshida M, et al. (2014) Controlling charge-density-wave states in nano-thick crystals of 1T-TaS$_2$. *Sci Rep* 4:7302.
5. Yu Y, et al. (2015) Gate-tunable phase transitions in thin flakes of 1T-TaS$_2$. *Nat Nanotechnol* 10(3):270–276.
6. Hollander MJ, et al. (2015) Electrically driven reversible insulator-metal phase transition in 1T-TaS$_2$. *Nano Lett* 15(3):1861–1866.
7. Vaskivskyi I, et al. (2014) Fast non-thermal switching between macroscopic charge-ordered quantum states induced by charge injection. arXiv:1409.3794.
8. Yoshida M, Suzuki R, Zhang Y, Nakano M, Iwasa Y (2015) Memristive phase switching in two-dimensional crystals. arXiv:1505.04038.
9. Wilson JA, DiSalvo FJ, Mahajan S (1975) Charge-density waves and superlattices in the metallic layered transition metal dichalcogenides. *Adv Phys* 24(2):117–201.
10. Ishiguro T, Sato H (1991) Electron microscopy of phase transformations in 1T-TaS$_2$. *Phys Rev B* 44(5):2046–2060.
11. Wu XL, Lieber CM (1989) Hexagonal domain-like charge density wave phase of TaS2 determined by scanning tunneling microscopy. *Science* 243(4899):1703–1705.
12. Burk B, Thomson RE, Zettl A, Clarke J (1991) Charge-density-wave domains in 1T-TaS$_2$ observed by satellite structure in scanning-tunneling-microscopy images. *Phys Rev Lett* 66(23):3040–3043.
13. Wu XL, Lieber CM (1990) Direct observation of growth and melting of the hexagonal-domain charge-density-wave phase in 1T-TaS$_2$ by scanning tunneling microscopy. *Phys Rev Lett* 64(10):1150–1153.
14. Thomson RE, Burk B, Zettl A, Clarke J (1994) Scanning tunneling microscopy of the charge-density-wave structure in 1T-TaS$_2$. *Phys Rev B* 49(24):16899–16916.
15. Spijkerman A, deBoer JL, Meetsma A, Wiegers GA, vanSmaalen S (1997) X-ray crystal-structure refinement of the nearly commensurate phase of **1T−TaS$_2$** in **(3+2)**-dimensional superspace. *Phys Rev B* 56(21):13757.
16. Wang L, et al. (2013) One-dimensional electrical contact to a two-dimensional material. *Science* 342(6158):614–617.
17. Grüner G (1994) *Density Waves in Solids* (Perseus Publishing, Cambridge, MA).
18. Millan Mc (1975) W. L. Landau theory of charge-density waves in transition-metal dichalcogenides. *Phys Rev B* 12(4):1187–1196.
19. Millan Mc (1976) W. L. Theory of discommensurations and the commensurate-incommensurate charge-density-wave phase transition. *Phys Rev B* 14(4): 1496–1502.
20. Rice TM, Whitehouse S, Littlewood P (1981) Impurity pinning of discommensurations in charge-density waves. *Phys Rev B* 24(5):2751–2759.
21. Giambattista B, Slough CG, McNairy WW, Coleman RV (1990) Scanning tunneling microscopy of atoms and charge-density waves in 1T-TaS$_2$, 1T-TaSe$_2$, and 1T-VSe$_2$. *Phys Rev B* 41(14):10082–10103.
22. Arguello CJ, et al. (2014) Visualizing the charge density wave transition in 2H-NbSe$_2$ in real space. *Phys Rev B* 89(23):235115.
23. Tanda S, Sambongi T, Tani T, Tanaka S (1984) X-ray study of charge density wave structure in 1T-TaS$_2$. *J Phys Soc Jpn* 53(2):476–479.
24. Geim AK, Grigorieva IV (2013) Van der Waals heterostructures. *Nature* 499(7459): 419–425.
25. Nattermann T (1985) Ising domain wall in a random pinning potential. *J Phys C Solid State Phys* 18(36):6661–6679.

PHYSICS